

Suppression of axionic charge density wave and onset of superconductivity in the chiral Weyl semimetal Ta₂Se₈I

Qing-Ge Mu,¹ Dennis Nenno,^{1,2} Yan-Peng Qi,^{1,3} Feng-Ren Fan,¹ Cuiying Pei,³ Moaz ElGhazali,¹ Johannes Gooth,^{1,4} Claudia Felser,¹ Prineha Narang^{2,*} and Sergey Medvedev^{1,†}

¹Max Planck Institute for Chemical Physics of Solids, 01187 Dresden, Germany

²John A. Paulson School of Engineering and Applied Sciences, Harvard University, Cambridge, Massachusetts 02138, USA

³School of Physical Science and Technology, ShanghaiTech University, Shanghai 201210, China

⁴Institut für Festkörper- und Materialphysik, Technische Universität Dresden, 01069 Dresden, Germany



(Received 16 March 2021; accepted 8 July 2021; published 9 August 2021)

A Weyl semimetal with strong electron-phonon interaction can show axionic coupling in its insulator state at low temperatures, owing to the formation of a charge density wave (CDW). Such a CDW emerges in the linear-chain-compound Weyl semimetal Ta₂Se₈I below 263 K, resulting in the appearance of the dynamical condensed-matter axion quasiparticle. In this paper, we demonstrate that the interchain coupling in Ta₂Se₈I can be varied to suppress the CDW formation with pressure, while retaining the Weyl semimetal phase at high temperatures. Above 17 GPa, the Weyl semimetal phase does not survive, and we induce superconductivity, due to the amorphization of the iodine sublattice. Structurally, the quasi-one-dimensional Ta-Se chains remain intact and provide a channel for superconductivity. We highlight that our results show a near-complete suppression of the gap induced by the axionic charge density wave at pressures inaccessible to previous studies. Including this CDW phase, our experiments and theoretical predictions and analysis reveal the complete phase diagram of Ta₂Se₈I and its relationship to the nearby superconducting state. The results demonstrate Ta₂Se₈I to be a distinctively versatile platform for exploring correlated topological states.

DOI: [10.1103/PhysRevMaterials.5.084201](https://doi.org/10.1103/PhysRevMaterials.5.084201)

I. INTRODUCTION

Topological materials are typically well described by the band theory of noninteracting electrons [1–3]. However, for materials with strong electron-phonon interactions, this description is no longer valid [4–7]. Instead, their topological ground state merely emerges from minimizing the energy of the strongly coupled electron-phonon system. A Weyl semimetal with strong electron-phonon interactions, for example, can show axionic coupling in its insulator state at low temperatures, owing to the formation of a charge density wave (CDW) [6–8]. In their parent state, Weyl semimetals are materials in which low-energy electronic quasiparticles behave as chiral relativistic fermions without rest mass, known as Weyl fermions [3]. Weyl fermions exist at isolated crossing points of the conduction and valence bands—the Weyl nodes—and their energy can be approximated with a linear dispersion relation. By turning on strong electron-phonon interactions, a CDW can emerge that links two Weyl nodes of different

chiralities and gaps the Weyl crossing points. A CDW is an ordered quantum fluid of electrons that forms a standing wave pattern along the atomic chains. It is characterized by a gap in the single-particle excitation spectrum and by a gapless electrical-current-carrying collective mode, the phason [9,10]. In Weyl semimetals, the phason of a charge density wave state is an axion, which couples to an electromagnetic field in the topological $\theta E \cdot B$ term [6,11]. Recently, signatures of such an axionic CDW were found in the linear-chain-compound Weyl semimetal, resulting in the observation of the dynamical condensed-matter axion quasiparticle [8]. Ta₂Se₈I is a quasi-one-dimensional (Q1D) material with a body-centered tetragonal lattice [see Fig. 3(c)]. The Ta atoms are surrounded by Se₄ rectangles and form chains aligned along the c axis. These chains are separated by I ions. Upon cooling down below $T_{\text{CDW}} = 263$ K, Ta₂Se₈I undergoes a CDW transition at ambient pressure [12–17]. The wave vector of the CDW in Ta₂Se₈I is incommensurate with the lattice, and the phason is generally pinned to impurities. Therefore only upon applying a certain threshold electric field (above which the electric force overcomes the pinning forces) is the phason depinned and free to slide over the lattice, thereby contributing to the electrical conduction. The resulting conduction behavior is strongly nonlinear and is a characteristic feature of the CDW state. Ta₂Se₈I is so far the only material in which a combination of charge density wave and chiral anomaly has been demonstrated, and experimental conditions sensitively influence the observability of this phase [8,18]. In order to map out the region of existence for this axionic charge density

*prineha@seas.harvard.edu

†sergiy.medvedev@cpfs.mpg.de

Published by the American Physical Society under the terms of the [Creative Commons Attribution 4.0 International license](https://creativecommons.org/licenses/by/4.0/). Further distribution of this work must maintain attribution to the author(s) and the published article's title, journal citation, and DOI. Open access publication funded by the Max Planck Society.

wave, we combine magnetotransport measurements, Raman spectroscopy, and *ab initio* calculations to assess its phase diagram. For pressures below the superconducting transition, we show a near-complete suppression of the CDW that has remained elusive in prior work. Above the critical pressure at which we observe superconductivity, our results highlight that the TaSe₄ building blocks of the quasi-one-dimensional chains survive, while the rest of the structure becomes amorphous. The present study accesses the phase diagram beyond what is known about this unique compound and paves the way toward a more microscopic understanding of its dynamics.

II. EXPERIMENTAL DETAILS

Needlelike single crystals of Ta₂Se₈I were obtained by the chemical vapor transport method. The same batch of crystals was used as in Ref. [8]. For high-pressure electrical transport property and Raman spectroscopy measurements a nonmagnetic diamond anvil cell (DAC) with 500- μ m culet was used with pressure up to 50 GPa. The electrical leads were fabricated from 5- μ m-thick Pt foil and insulated from the Re gasket with a cubic-BN-epoxy mixture. The temperature dependence of electrical resistivity and voltage-current (V-I) characteristics were collected on needlelike crystals with a standard four-probe method using NaCl as the pressure-transmitting medium (PTM), and the electric current was along the *c* axis. Hall measurements were carried out with the van der Pauw method, and the sample chamber adopts a 200- μ m diameter and 40- μ m thickness which is only filled with crystals. Electrical transport property measurements were performed on a Quantum Design physical property measurement system (PPMS-9) down to 1.8 K with magnetic field ranging from -9 to 9 T. Raman spectra were recorded using a customary confocal micro-Raman spectrometer with a HeNe laser as the excitation source and a single-grating spectrograph with 1 cm⁻¹ resolution. Pressure was measured with an accuracy of ≈ 0.1 GPa using the ruby luminescence method.

In situ high-pressure x-ray diffraction (XRD) measurements up to 45 GPa were performed at beamline 15U at Shanghai Synchrotron Radiation Facility (x-ray wavelength $\lambda = 0.6199$ Å). A symmetric DAC with anvil culet sizes of 200 μ m as well as Re gaskets was used. Silicon oil was used as a quasihydrostatic PTM, and pressure was determined by the ruby luminescence method. The two-dimensional diffraction images were analyzed using DIOPTAS software. Rietveld refinements on crystal structures under high pressure were performed using General Structure Analysis System (GSAS) and the graphical user interface package EXPGUI.

The density function calculations for the Raman spectra and the electronic ground state in the Weyl semimetal phase, including the crystal-structure optimization and force-constant calculations, are performed by using the Vienna *ab initio* simulation package (VASP) with the Perdew-Burke-Ernzerhof (PBE) generalized gradient approximation (GGA) functional [19–21]. The projector augmented wave (PAW) method is used, and we adapt the experimental lattice parameters for simulations under pressure, only relaxing the ionic positions [22]. The energy cutoff is set to be 400 eV. A $5 \times 5 \times 5$ Monkhorst-Pack k-point grid is used for the

crystal-structure optimization, and a Γ -only point is used for force-constant calculation. The crystal structure is fully optimized until the force on each atom is smaller than 0.001 eV/Å. Based on this optimized structure, a $2 \times 2 \times 1$ supercell (176 atoms) is used to calculate the phonon spectra, following, in part, Ref. [23]. The force constants are calculated using the finite-displacement method, and the phonon calculations are performed by using PHONOPY [24].

III. SUPPRESSION OF THE CDW TRANSITION

We first map the transition temperature of the charge density wave under pressure using resistivity measurements. Figure 1(a) shows the single-particle electrical resistivity ρ of Ta₂Se₈I as a function of temperature *T* at various pressures *P* up to 10.4 GPa. At low *P* (1.4 and 6.6 GPa), each $\rho(T)$ exhibits a faint kink, i.e., a peak in its derivative [25], at particular temperatures T_{CDW} , indicative of the formation of the CDW [8]. The CDW-transition temperature of our samples at ambient *P* is $T_{\text{CDW}} = 263$ K [8], in good agreement with existing literature. With increasing pressure, we observe that the T_{CDW} first increases slightly until 1.4 GPa to 267 K but is then suppressed down to 204 K at 6.6 GPa [Fig. 1(a)]. This observed increase at low pressures is in agreement with previous reports [14,29]. Consistent with a sliding phason mode, we observe nonlinearity in the V-I curves below T_{CDW} at high bias currents, that is, high voltages [Fig. 1(d)]. For $P > 10$ GPa, the signature of the CDW transition in $\rho(T)$ is blurred out, but the crossover from linear V-I characteristics at high *T* to nonlinear V-I characteristics at low *T* remains observable [Figs. 1(e) and 1(f)]. Hence, in order to obtain the transition temperature for all pressures investigated, we use the onset temperature T_{on} of the nonlinear behavior in the V-I characteristic as a measure for T_{CDW} (see Supplemental Material for details). This procedure is justified by the experiments below 6.6 GPa, for which the independently determined T_{CDW} and T_{on} match, and allows us to go beyond the territory of phase diagrams in previous studies and to observe the near closing of the gap induced by the charge density wave [10].

Consistently, we find that $T_{\text{CDW}} (= T_{\text{on}})$ for pressures above 6.6 GPa decreases with increasing *P*. Finally, the V-I characteristic becomes linear at the lowest temperature, 2 K, investigated as the pressure is increased to 17 GPa [Fig. 1(g)], indicating the complete suppression of CDW formation. Hall measurements above T_{CDW} show that the carrier concentration increases with increasing *P* (Supplemental Fig. S2), indicating an enhancement of the Fermi-surface area when *P* is enhanced. This observation suggests that the Weyl points move away from the Fermi level for increasing pressure and potential contributions due to interband coupling. To gain more insights into the CDW state below T_{CDW} , we fit the single particle $\rho(T)$ in this temperature regime with a thermal activation law,

$$\rho(T) \propto \exp\left(\frac{\Delta E}{2k_{\text{B}}T}\right), \quad (1)$$

with the energy gap ΔE and the Boltzmann constant $k_{\text{B}}T$ (Supplemental Fig. S3). The estimated single-particle gap at low temperature decreases with increasing pressure from $\Delta E = (259 \pm 14)$ meV at ambient pressure to $\Delta E =$

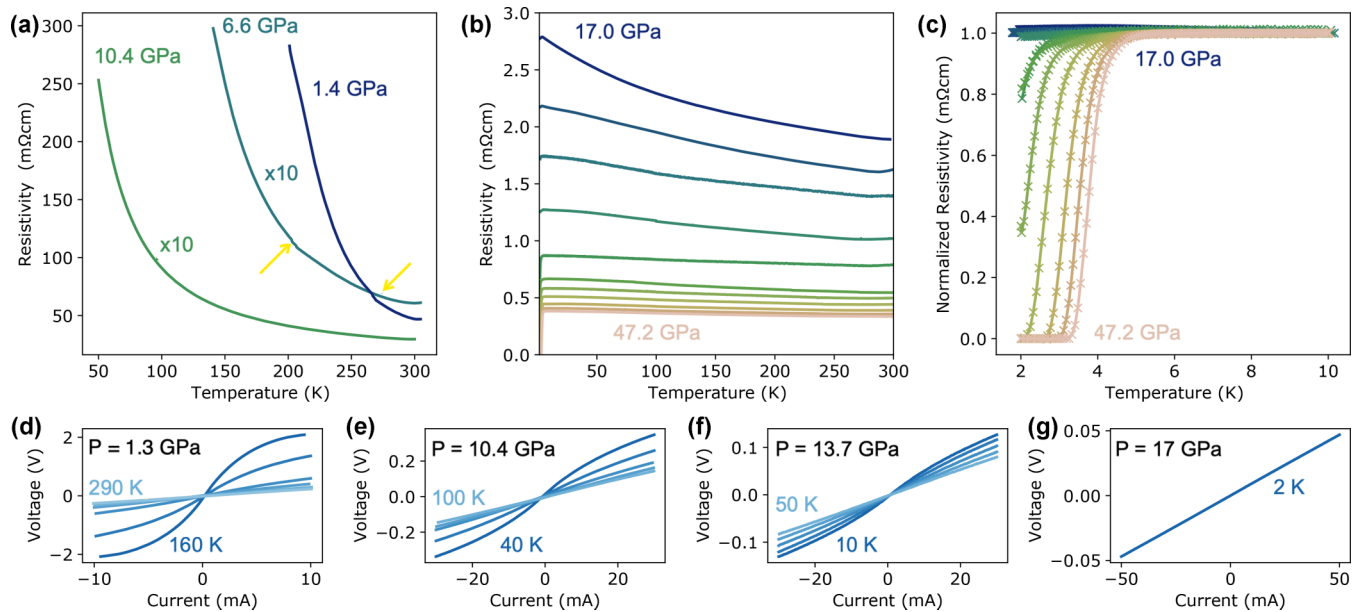


FIG. 1. Electrical transport in $\text{Ta}_2\text{Se}_8\text{I}$ under pressure. (a) Electrical resistivity vs temperature of $\text{Ta}_2\text{Se}_8\text{I}$; due to the formation of a charge density wave, an anomaly (indicated with yellow arrows) is visible at low pressures. The V-I characteristic switches from linear behavior (Ohmic) at high temperatures to nonlinear behavior by cooling below the T_{CDW} , which is a signature of sliding CDW transport. At higher pressures, the kink in the resistivity curves is smeared out [resistivity curve at 10.4 GPa in (a)]. The V-I characteristics, however, are demonstrating the switch to nonlinear behavior at high pressures for progressively lower temperatures [(d)–(f)]. Finally, the V-I characteristic remains linear down to the lowest temperature as pressure increases to 17 GPa (g), indicating the complete suppression of CDW formation. A drop in resistivity is observed at low temperature in resistivity curves as pressure increases further beyond the suppression of CDW formation (b), which suggests the onset of a superconducting transition. The superconducting state is clearly observed at higher pressures, with the resistivity dropping abruptly to zero (c) while the resistivity in the normal state demonstrates rather semimetallic character (b). The T_c keeps increasing monotonically with further increase in pressure and reaches 4.5 K at the highest pressure, 47.2 GPa.

(18.3 ± 0.03) meV at 10.4 GPa, again, consistent with the decreasing T_{CDW} [8].

IV. PRESSURE-INDUCED SUPERCONDUCTIVITY

Remarkably, above $P \sim 17$ GPa—the pressure where the CDW is suppressed—we observe a drop in $\rho(T)$ at low temperatures [Fig. 1(b)], indicating the onset of a superconducting transition. The superconducting state is clearly observed at higher pressures, with the single-particle resistivity dropping abruptly to zero when reaching the transition temperature T_c [Fig. 1(c)]. With increasing pressure, T_c keeps increasing monotonically and is 4.5 K at our maximum pressure of 47.2 GPa [25]. The state above T_c remains semimetallic [Fig. 1(b)]. Observations of pressure-induced superconductivity in $\text{Ta}_2\text{Se}_8\text{I}$ are in accordance with the results obtained on a number of Q1D transition metal chalcogenides in which suppression of the CDW state leads to the emergence of superconductivity [29–34]. We find that the superconductivity in $\text{Ta}_2\text{Se}_8\text{I}$ emerges only after the CDW state is completely suppressed, while the superconductivity and CDW transition coexist in related compounds, e.g., ZrTe_3 , orthorhombic TaS_3 (o- TaS_3), and NbSe_3 [30,31,33]. Such coexistence of superconductivity and CDW transition in o- TaS_3 is proposed to be related to the existence of a quantum critical point, a point at which the CDW-transition temperature is driven to zero by pressure [31]. Quantum fluctuations diverge at this point and might induce superconductivity with dome-shaped pressure

dependence of T_c in which maximum T_c appears around this quantum critical point. In $\text{Ta}_2\text{Se}_8\text{I}$, however, pressure drives the system farther away from the quantum critical point while the T_c continuously increases. These results show that maxima in the value of T_c in such systems might be obtained by going farther away from CDW instability and that a domelike shape for pressure dependence of T_c can be obtained without relation to CDW order [35].

V. RAMAN SPECTROSCOPY AND X-RAY DIFFRACTION STUDIES

To gain a deeper understanding of the different states in the pressure phase diagram of $\text{Ta}_2\text{Se}_8\text{I}$, we performed pressure-dependent Raman spectroscopy and synchrotron x-ray diffraction studies. The resulting spectra at selected pressures are shown in Fig. 2(a) and are consistent with previous reports [36–39]. Up to ~ 18 GPa, the Raman spectra of $\text{Ta}_2\text{Se}_8\text{I}$ become increasingly asymmetric with higher pressure, but the crystal structure remains stable. At pressures around 7 GPa, the Raman spectra demonstrate splitting of selected modes (Fig. 2), which can indicate a possible structural phase transition. However, the peak splitting is observed only for selected types of modes, and there are no sudden changes in the profile of the spectrum upon pressure increase. Therefore the possibility of a major structural transition can be ruled out since such a transition is usually associated with drastic changes in the Raman spectra due to the deformation

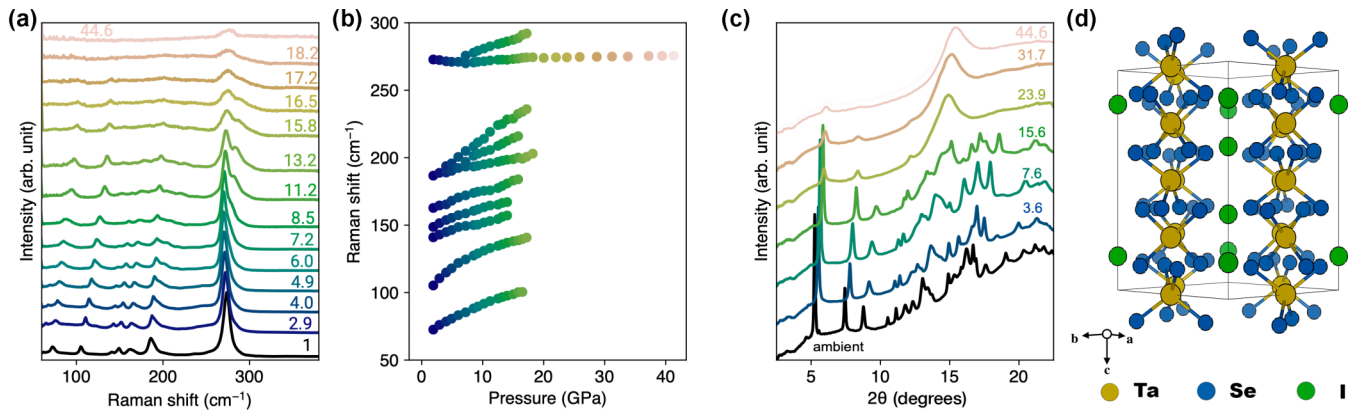


FIG. 2. Pressure effect on the structure of $\text{Ta}_2\text{Se}_8\text{I}$. Upon applying pressure, all observed Raman peaks (a) except the one located at $\sim 274 \text{ cm}^{-1}$ shift to higher frequencies (b) demonstrating normal stiffening behavior upon compression. Disappearance of the majority of Raman peaks at pressures above $\sim 18 \text{ GPa}$ (a) indicates pressure-induced amorphization of $\text{Ta}_2\text{Se}_8\text{I}$. *In situ* synchrotron XRD patterns of $\text{Ta}_2\text{Se}_8\text{I}$ (c) demonstrate the pressure-induced amorphization as pressure approaches $\sim 20 \text{ GPa}$. The strongest Raman peak (located at $\sim 274 \text{ cm}^{-1}$) corresponding to the intrachain Se-Se stretching vibrations can be observed up to the highest pressures in these experiments [(a) and (b)] indicating the preservation of the TaSe_4 units as building blocks of local order in the high-pressure amorphous phase of $\text{Ta}_2\text{Se}_8\text{I}$. The conventional cell of $\text{Ta}_2\text{Se}_8\text{I}$ crystallizes in space group 97 (d).

of the Brillouin zone. On the one hand, considering that the peaks consist of multiple vibrational modes (Supplemental Table S1; the atomic characters of each mode are shown in Supplemental Fig. S6), the peak splitting can also be ascribed to different pressure coefficients of the respective modes. On the other hand, this splitting might be indicative of the distortion of the Ta-Ta distances within the chains (which are uniform at ambient pressure) resulting in the continuous distortion of the initially slightly distorted rectangular Ta-Se antiprisms, similar to the case of $(\text{NbSe}_4)_3\text{I}$ with slightly distorted Nb-Nb distances in which corresponding Raman peaks are split [36]. All the vibrational modes exhibit blue shift except the strongest one (located at $\sim 274 \text{ cm}^{-1}$) [Fig. 2(b)], which is assigned to the intrachain Se-Se stretching vibrations. It is worth noting the remarkable similarity of the unusual nonmonotonic behavior of the Se-Se stretching vibrations in $\text{Ta}_2\text{Se}_8\text{I}$ (Fig. 2) and the corresponding Raman peak in Q1D $o\text{-TaS}_3$ [40]. This similarity is indicative for the generality in the structural response to external pressure in Q1D transition metal chalcogenides, which remains unexplored so far. Pressure-dependent x-ray diffraction studies [Fig. 2(c)] further demonstrate the stability of the $\text{Ta}_2\text{Se}_8\text{I}$ structure up to $\sim 20 \text{ GPa}$, as no additional peaks or splittings are observed in the diffraction patterns.

For pressures above $\sim 18 \text{ GPa}$, however, only the strongest high-frequency peak persists in the experimental spectra, and this change remains after decompression, indicating diminishing crystal order at least in part of the $\text{Ta}_2\text{Se}_8\text{I}$ sample. This pressure-induced amorphization is observed also by the evolution of x-ray diffraction patterns in which the disappearance of the sample Bragg peaks and the formation of broad amorphous halo patterns are observed at pressures above $\sim 20 \text{ GPa}$ [Fig. 2(c)]. The persistent, isolated Raman peak corresponding to the intrachain Se-Se stretching vibrations can be observed up to the highest pressures (above 40 GPa), indicating the preservation of the TaSe_4 units as building blocks of local order in the high-pressure amorphous

phase of $\text{Ta}_2\text{Se}_8\text{I}$. The decomposition of the $\text{Ta}_2\text{Se}_8\text{I}$ crystal structure might be excluded, as no Raman modes that could not be assigned to the parent material were observed. Thus the persistence of the strongest peak in the spectra and its monotonic behavior over frequency indicates that the quasi-one-dimensional Ta-Se chains of $\text{Ta}_2\text{Se}_8\text{I}$ remain intact up to the highest pressure [39]. However, partial loss of crystallinity (or pressure-induced amorphization) cannot be excluded. Structural studies of $\text{Ta}_2\text{Se}_8\text{I}$ under such high pressures would be of importance for further understanding of the properties of this material.

VI. AB INITIO CALCULATIONS

Further insights into the semimetal and CDW state for pressures below the superconducting transition emerge from our *ab initio* calculations. Our results for the electronic band structure for the high-temperature phase of $\text{Ta}_2\text{Se}_8\text{I}$ are summarized for various pressures in Fig. 3. Consistent with the conclusion from the Hall measurements, compressing the unit cell leads to a shift of the Ta $d_{3z^2-r^2}$ towards lower energies, which moves the Weyl points away from the Fermi level, reducing the net chiral charge and increasing the density of states at the Fermi level [41,42]. At the same time, the interchain coupling increases up until I p bands hybridize at the Fermi level above 15 GPa . At this point, we expect the CDW mechanism outlined in Refs. [41] and [23] to break down, as the charge density wave vector is incommensurate with the Fermi-surface nesting, i.e., $2k_F \neq q_{\parallel}^{\text{CDW}}$, and consequently, the axionic magnetoresponse observed in the gapped phase should vanish [8]. We additionally calculate the phonon dispersions in the low-temperature regime (Supplemental Fig. S5) that reveal the structural instability that leads to the formation of the CDW below 16 GPa , which was observed for ambient pressure in Refs. [23] and [43].

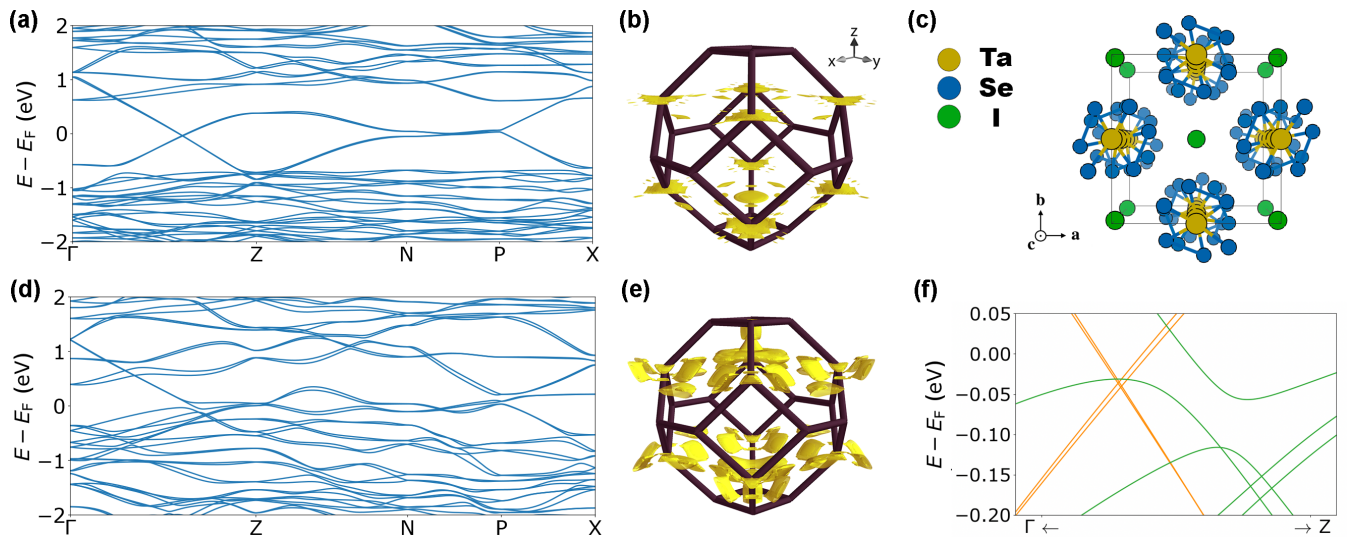


FIG. 3. *Ab initio* electronic band structure in the high-symmetry phase of $\text{Ta}_2\text{Se}_8\text{I}$ at 7.6 GPa (a) and 15.6 GPa (d) incorporating the experimental lattice parameters. While the Fermi surface at 7.6 GPa (b) does not yet deviate drastically from quasi-one-dimensional behavior, or from the result at ambient pressure, bands with contributions from the iodine atoms add to the three-dimensionality at 15.6 GPa (e). The conventional cell of $\text{Ta}_2\text{Se}_8\text{I}$ displays Ta-Se chains spaced by iodine atoms (c). Increasing pressure leads to the Weyl point manifold on the $\Gamma \rightarrow Z$ axis moving away from the Fermi level at 7.6 GPa (orange lines) and 15.6 GPa (green lines) (f).

VII. CONCLUSION

The complete phase diagram, created with newly discovered physics in $\text{Ta}_2\text{Se}_8\text{I}$ as well as our calculations and analysis, is shown in Fig. 4 [8,39]. At ambient pressure, $\text{Ta}_2\text{Se}_8\text{I}$ is a Weyl semimetal that exhibits a phase transition

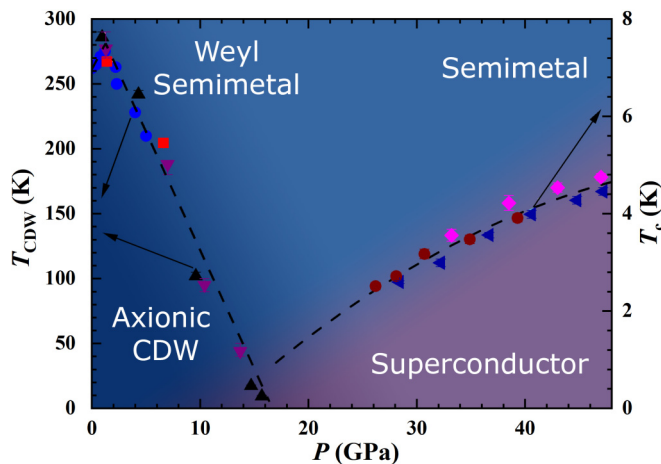


FIG. 4. The phase diagram displaying the pressure effects on CDW transition and superconductivity with pressure up to 47.2 GPa on several samples. The solid blue circles are the CDW-transition temperatures reported by Refs. [29] and [14]. The red squares are extracted from resistivity measurements, and both purple and black triangles are from the V-I characteristics. For superconductivity, different symbols represent the onset T_c from different samples. Error bars of T_{CDW} from V-I curves are based on the temperature step. Error bars of T_{CDW} from resistivity and superconducting T_c come from the average of multiple readings and appear smaller than the data symbols.

to an axionic CDW state below $T_{\text{CDW}} = 263$ K [8]. Our data show that with increasing pressure, the transition temperature and, consequently, the gap size are successively reduced. At ~ 17 GPa, the CDW state is fully suppressed, the Q1D behavior vanishes, and a partial amorphization accompanied with a superconducting transition emerges. The critical temperature continuously increases up to 4.5 K at the highest pressure applied (47.2 GPa). Looking ahead, structural studies would deepen the understanding of the properties of $\text{Ta}_2\text{Se}_8\text{I}$ and similar yet-to-be-observed axionic materials under such high pressures.

ACKNOWLEDGMENTS

This work is financially supported by ERC Advanced Grant No. 742068, “TOPMAT” and the DARPA DSO under the Driven Nonequilibrium Quantum Systems (DRINQS) program, Grant No. D18AC00014. D.N. is partially supported by the Department of Energy “Photonics at Thermodynamic Limits” Energy Frontier Research Center under Grant No. DE-SC0019140. Y.-P.Q. acknowledges the support from the National Key Research and Development Program of China (Grant No. 2018YFA0704300) and the National Natural Science Foundation of China (Grants No. U1932217 and No. 11974246). We also thank the staff from beamline BL15U1 at the Shanghai Synchrotron Radiation Facility for assistance during data collection. P.N. is supported by the Moore Inventor Fellows program through Grant No. GBMF8048 from the Gordon and Betty Moore Foundation. This research used resources of the National Energy Research Scientific Computing Center (NERSC), a U.S. Department of Energy Office of Science User Facility operated under Contract No. DE-AC02-05CH11231.

- [1] X.-L. Qi, T. L. Hughes, and S.-C. Zhang, *Phys. Rev. B* **78**, 195424 (2008).
- [2] M. Z. Hasan and C. L. Kane, *Rev. Mod. Phys.* **82**, 3045 (2010).
- [3] N. P. Armitage, E. J. Mele, and A. Vishwanath, *Rev. Mod. Phys.* **90**, 015001 (2018).
- [4] K.-Y. Yang, Y.-M. Lu, and Y. Ran, *Phys. Rev. B* **84**, 075129 (2011).
- [5] M. Laubach, C. Platt, R. Thomale, T. Neupert, and S. Rachel, *Phys. Rev. B* **94**, 241102(R) (2016).
- [6] Z. Wang and S.-C. Zhang, *Phys. Rev. B* **87**, 161107(R) (2013).
- [7] Y. Tanaka, R. Takahashi, T. Zhang, and S. Murakami, *Phys. Rev. Res.* **2**, 043274 (2020).
- [8] J. Gooth, B. Bradlyn, S. Honnali, C. Schindler, N. Kumar, J. Noky, Y. Qi, C. Shekhar, Y. Sun, Z. Wang, B. A. Bernevig, and C. Felser, *Nature (London)* **575**, 315 (2019).
- [9] P. W. Anderson, *Basic Notions of Condensed Matter Physics* (CRC, Ann Arbor, 2018).
- [10] P. Monceau, *Adv. Phys.* **61**, 325 (2012).
- [11] D. M. Nenko, C. A. C. Garcia, J. Gooth, C. Felser, and P. Narang, *Nat. Rev. Phys.* **2**, 682 (2020).
- [12] H. Fujishita, M. Sato, and S. Hoshino, *J. Phys. C: Solid State Phys.* **18**, 1105 (1985).
- [13] L. Forró, J. Cooper, A. Janossy, and M. Maki, *Solid State Commun.* **62**, 715 (1987).
- [14] L. Forró, H. Mutka, S. Bouffard, J. Morillo, and A. Jánossy, in *Charge Density Waves in Solids* (Springer, New York, 1985), pp. 361–365.
- [15] J. Lorenzo, *J. Phys.: Condens. Matter* **10**, 5039 (1998).
- [16] L. Nemeth, P. Matus, G. Kriza, and B. Alavi, *Synth. Met.* **120**, 1007 (2001).
- [17] C. Tournier-Colletta, L. Moreschini, G. Autès, S. Moser, A. Crepaldi, H. Berger, A. L. Walter, K. S. Kim, A. Bostwick, P. Monceau, E. Rotenberg, O. V. Yazyev, and M. Grioni, *Phys. Rev. Lett.* **110**, 236401 (2013).
- [18] I. A. Cohn, S. G. Zybtev, A. P. Orlov, and S. V. Zaitsev-Zotov, *JETP Lett.* **112**, 88 (2020).
- [19] G. Kresse and J. Hafner, *Phys. Rev. B* **48**, 13115 (1993).
- [20] G. Kresse and J. Furthmüller, *Phys. Rev. B* **54**, 11169 (1996).
- [21] J. P. Perdew, K. Burke, and M. Ernzerhof, *Phys. Rev. Lett.* **77**, 3865 (1996).
- [22] P. E. Blöchl, *Phys. Rev. B* **50**, 17953 (1994).
- [23] Y. Zhang, L.-F. Lin, A. Moreo, S. Dong, and E. Dagotto, *Phys. Rev. B* **101**, 174106 (2020).
- [24] A. Togo and I. Tanaka, *Scr. Mater.* **108**, 1 (2015).
- [25] See Supplemental Material at <http://link.aps.org/supplemental/10.1103/PhysRevMaterials.5.084201> for further details on the superconducting state, which includes Refs. [26–28].
- [26] A. Gurevich, *Phys. Rev. B* **67**, 184515 (2003).
- [27] S. Khim, B. Lee, J. W. Kim, E. S. Choi, G. R. Stewart, and K. H. Kim, *Phys. Rev. B* **84**, 104502 (2011).
- [28] Z. Z. Wang, M. Saint-Lager, P. Monceau, M. Renard, P. Gressier, A. Meerschaut, L. Guemas, and J. Rouxel, *Solid State Commun.* **46**, 325 (1983).
- [29] M. Nunez-Regueiro, J.-M. Mignot, M. Jaime, D. Castello, and P. Monceau, *Synth. Met.* **56**, 2653 (1993).
- [30] R. Yomo, K. Yamaya, M. Abliz, M. Hedo, and Y. Uwatoko, *Phys. Rev. B* **71**, 132508 (2005).
- [31] M. Monteverde, J. Lorenzana, P. Monceau, and M. Núñez Regueiro, *Phys. Rev. B* **88**, 180504(R) (2013).
- [32] X. Yang, Y. Zhou, M. Wang, H. Bai, X. Chen, C. An, Y. Zhou, Q. Chen, Y. Li, Z. Wang, J. Chen, C. Cao, Y. Li, Y. Zhou, Z. Yang, and Z.-A. Xu, *Sci. Rep.* **8**, 6298 (2018).
- [33] S. Yasuzuka, K. Murata, T. Fujimoto, M. Shimotori, and K. Yamaya, *J. Phys. Soc. Jpn.* **74**, 1782 (2005).
- [34] K. Gu, R. A. Susilo, F. Ke, W. Deng, Y. Wang, L. Zhang, H. Xiao, and B. Chen, *J. Phys.: Condens. Matter* **30**, 385701 (2018).
- [35] V. G. Tissen, M. R. Osorio, J. P. Brison, N. M. Nemes, M. García-Hernández, L. Cario, P. Rodière, S. Vieira, and H. Suderow, *Phys. Rev. B* **87**, 134502 (2013).
- [36] T. Ikari and F. Lévy, *J. Phys. C: Solid State Phys.* **18**, L1109 (1985).
- [37] T. Sekine, T. Seino, M. Izumi, and E. Matsuura, *Solid State Commun.* **53**, 767 (1985).
- [38] A. Zwick, M. Renucci, P. Gressier, and A. Meerschaut, *Solid State Commun.* **56**, 947 (1985).
- [39] C. An, Y. Zhou, C. Chen, F. Fei, F. Song, C. Park, J. Zhou, H.-G. Rubahn, V. V. Moshchalkov, X. Chen, G. Zhang, and Z. Yang, *Adv. Mater.* **32**, 2002352 (2020).
- [40] K. Wu, *J. Phys. Chem. C* **121**, 28187 (2017).
- [41] W. Shi, B. J. Wieder, H. L. Meyerheim, Y. Sun, Y. Zhang, Y. Li, L. Shen, Y. Qi, L. Yang, J. Jena, P. Werner, K. Koepf, S. Parkin, Y. Chen, C. Felser, B. A. Bernevig, and Z. Wang, *Nat. Phys.* **17**, 381 (2021).
- [42] X.-P. Li, K. Deng, B. Fu, Y. K. Li, D.-S. Ma, J. F. Han, J. Zhou, S. Zhou, and Y. Yao, *Phys. Rev. B* **103**, L081402 (2021).
- [43] Y. Yin, J. Coulter, C. J. Ciccarino, and P. Narang, *Phys. Rev. Mater.* **4**, 104001 (2020).